LJMU Research Online

Gkantou, M, Theofanous, M, Wang, J, Baniotopoulos, C and Gardner, L

 Behaviour and design of high-strength steel cross-sections under combined loading

http://researchonline.ljmu.ac.uk/9183/

Article

For more information please contact researchonline@ljmu.ac.uk

http://researchonline.ljmu.ac.uk/

Behaviour and design of high strength steel cross-sections under combined loading

Gkantou M[a], Theofanous M[a], Wang J[b], Baniotopoulos C[a] and Gardner L[b]

[a] University of Birmingham, Birmingham, UK

[b] Imperial College London, London, UK

Abstract

The behaviour of hot-rolled high strength steel (HSS) tubular sections under combined compression and uniaxial bending is investigated in the present paper both experimentally and numerically. The experimental programme encompassed a series of material coupon tests, initial geometric imperfection measurements, residual stress measurements and 12 tests on stub columns subjected to uniaxial eccentric compression. Numerical models were developed and validated against the experimental results. An extensive parametric study was then performed aiming to generate further structural performance data over a wider range of cross-section slendernesses, aspect ratios and applied eccentricities. The results have been utilised for the assessment of the applicability of relevant Eurocode provisions to HSS cross-sections under combined loading, and conclusions regarding the applicability of Eurocode interaction curves to S460 and S690 square and rectangular hollow sections have been presented.

Keywords: Eccentric compression; Eurocode 3; Experiments; High strength steel; Hollow sections; Local buckling; Local imperfection; N-M interaction; Testing

Notation

A	Cross-sectional area
A_c	Cross-sectional area of the coupon
A_{eff}	Effective cross-sectional area
b	Section width
CF	Compressive flat (coupon)
COV	Coefficient of variation
CP	Control point
$c/t\varepsilon$	Element slenderness
E	Young's modulus
e_0	Actual initial loading eccentricity
$e_{0,n}$	Nominal initial loading eccentricity
e'	Eccentricity generated due to second order effect
e_u'	Eccentricity at ultimate load generated due to second order effect
FE	Finite element
f_u	Ultimate tensile strength
f_y	Yield strength
h	Section depth
HSS	High strength steel
I	Second moment of area
L	Length
M_{el}	Elastic moment
M_{pl}	Plastic moment
M_u	Failure moment
$M_{u,exp}$	Experimentally obtained failure moment
$M_{u,FE}$	Numerically obtained failure moment
N_u	Failure load
$N_{u,exp}$	Experimentally obtained failure load
$N_{u,FE}$	Numerically obtained failure load

R_{exp}/R_{pred}	Ratio of experimental to predicted capacity
R_{FE}/R_{pred}	Ratio of FE to predicted capacity
RHS	Rectangular hollow section
r_i	Internal corner radius
SHS	Square hollow section
t	Thickness
TC	Tensile corner (coupon)
TF	Tensile flat (coupon)
W_{eff}	Elastic modulus of effective section
W_{el}	Elastic section modulus
W_{pl}	Plastic section modulus
β	Coefficient for prediction of imperfection amplitude
$\varepsilon_{concave}$	Strain on concave side of cross-section
ε_{convex}	Strain on convex side of cross-section
ε_{eng}	Engineering strain
ε_f	Strain at fracture
ε_{ln}^{pl}	Logarithmic plastic strain
ε_u	Strain at ultimate stress
σ_{cr}	Elastic local plate buckling stress
σ_{eng}	Engineering stress
σ_{true}	True stress
φ_u	Mean end-rotation at failure load
ψ	Ratio of stresses or strains across section depth
ω_0	Measured initial local geometric imperfection
ω_{DW}	Initial local geometric imperfection from Dawson and Walker model

1. Introduction

Over the last few decades, several studies have shown that there are potential benefits in using high strength steels (HSS) in building and bridge applications (Bjorhovde, 2004; Höglund et al., 2005). However, given that most international structural design standards (CAN/CSA-S16-01, 2001; GB 50017-2003, 2006; ANSI/AISC 360-10, 2010; AISI S100, 2012; AS 4100-A1, 2012) either do not cover high strength steels or adopt design methods identical to those for normal strength steels, there is a clear need for the development of comprehensive design guidance for HSS structures.

The European provisions for HSS structural design are set out in EN 1993-1-12 (2007), where additional rules for steels with yield strengths beyond 460 N/mm^2 and up to 700 N/mm^2 are specified. EN 1993-1-12 (2007) relaxes the requirements imposed on the strain hardening and ductility characteristics of HSS material, but, other than some specific restrictions (e.g. plastic design is not permitted), generally applies the same cross-section and member design rules as for conventional steel design by referring to EN 1993-1-1 (2014). There is however a clear need to fully verify and further develop these rules, and to extend the experimental database on HSS structural elements beyond that available when EN 1993-1-12 (2007) was published (McDermott, 1969; Usami and Fukumoto, 1984; Rasmussen and Hancock, 1992; Rasmussen and Hancock, 1995; Beg and Hladnik, 1996; Ricles et al., 1998; Yang and Hancock, 2004; Yang et al., 2004).

Recently, several researchers have investigated the member buckling behaviour of HSS long columns (Rasmussen and Hancock, 1995; Yang et al., 2004; Shi et al., 2012; Ban et al., 2013; Wang et al., 2014), the cross-sectional behaviour of HSS beams (McDermott, 1969; Usami and Fukumoto, 1984; Beg and Hladnik, 1996; Ricles et al., 1998; Lee et al., 2012; Wang et al., 2016) and stub columns (Usami and Fukumoto, 1984; Rasmussen and Hancock, 1992; Beg and Hladnik, 1996; Yang and Hancock, 2004; Yang and Hancock, 2006; Gao et al., 2009; Yoo et al., 2013; Shi et al., 2014; Gkantou et al., accepted), and have made recommendations regarding the structural design of HSS members, including revised slenderness limits, effective width equations and column buckling design curves. However, studies on HSS cross-sections under combined axial load and bending moment

(Kim et al., 2014) remain scarce. Similar studies on the structural response of eccentrically loaded stub columns have been recently reported for stainless steel sections (Zhao et al., 2015a; Zhao et al., 2015b; Arrayago and Real, 2015) and composite sections (Fujimoto et al., 2004; Sheehan et al., 2012).

A comprehensive experimental programme was undertaken in the Structures Laboratory at Imperial College London, focusing on the structural behaviour of hot-rolled HSS square and rectangular hollow sections (SHS and RHS). The overall programme comprised material coupon tests, geometric imperfection and residual stress measurements, stub column tests (Wang et al., 2017), 3-point and 4-point in-plane bending tests (Wang et al., 2016), and tests on cross-sections under combined loading, which are reported herein. In parallel with the experimental programme, a numerical study has also been conducted. The first step of the numerical study was to develop reliable finite element (FE) models capable of replicating the experimental findings; the second step was to use the validated models to generate further structural performance data over a wider range of local slendernesses and loading (i.e. combinations of axial load and bending moments). Finally, the combined experimental and numerical results were used to assess the accuracy of the design rules presented in EN 1993-1-12 (2007), which refer to EN 1993-1-1 (2014), for predicting the cross-section capacity of hot-finished HSS SHS and RHS under combined loading.

2. Experimental study

2.1. General

A total of 12 stub column specimens were tested under uniaxial eccentric compressive loads, to assess their structural behaviour under combined axial load and bending moments. The tested cross-sections were SHS 50×50×5 in grade S460 steel and SHS 50×50×5 and SHS 90×90×5.6 in grade S690 steel. Both the S460 and S690 specimens were hot-rolled seamless tubular sections, hollowed out by a piercing mill to the final shape, after which the S460 sections were normalised, whereas the S690 were quenched and tempered. The chemical composition and the tensile material properties of the tested specimens, as provided by the mill certificates, are presented in Tables 1 and 2 respectively. In

addition to the eccentric compression tests, corresponding material coupon tests, initial geometric imperfection measurements and residual stress measurements have also been conducted for each cross-section, as reported hereafter.

2.2. Material testing

A comprehensive coupon testing programme covering tensile flat, tensile corner and compressive flat coupons has been carried out on the studied cross-sections. The resulting material properties were used in the analysis of the combined loading test results and in the development of the numerical models of the tested specimens. For each cross-section, four flat coupons and one corner coupon were extracted from the locations indicated in Figure 1 and tested in tension. Additionally, one compressive flat coupon was also cut from a flat face of each cross-section. The tests were conducted in accordance with ISO 6892-1 (2009). Measured stress–strain curves from the coupon tests are displayed in Figures 2(a) and 2(b) for the S460 SHS 50×50×5 and S690 SHS 50×50×5 specimens respectively. It can be seen that both grades of material display a sharply defined yield point followed by a yield plateau; the S690 material generally exhibited less strain hardening and lower ductility than the S460 material. Key results from the coupon tests (tensile flat (TF), tensile corner (TC) and compressive flat (CF) coupons) are summarised in Table 3, where the material parameters reported are the Young's modulus E, the upper yield strength f_y, the ultimate tensile strength f_u, the tensile-to-yield stress ratio f_u/f_y, the strain at the ultimate tensile stress ε_u and the plastic strain at fracture ε_f, based on elongation over the standard gauge length equal to $5.65\sqrt{A_c}$, where A_c is the cross-sectional area of the coupon (ISO 6892-1, 2009). Further details of the experimental procedure and results are reported in Wang et al. (2017).

It should be noted that the TF results are the average results of the four tensile flat coupons. Since the corner coupons are observed to behave very similarly to their flat counterparts in terms of the shape of the stress–strain curve and the key material parameters, the average results from the flat coupon tests (TF results in Table 3) were used in the subsequent data analysis and numerical modelling of the combined loading tests.

2.3. Local imperfection and residual stress measurements

For structural elements prone to buckling, the presence of imperfections can have a strong influence on their behaviour and load-carrying capacity. Typical structural imperfections for steel members include geometric (global and local) imperfections and residual stresses. Including imperfections in finite element simulations enables accurate modelling of the structural response of the tested specimens. Since global imperfections are very small compared to the applied eccentricity in the present study and are only important for member buckling, which is not relevant for stub columns, only local imperfections and residual stress measurements are reported herein. The maximum recorded local geometric imperfections for the tested cross-sections, denoted ω_0, are reported in Table 4. The maximum measured longitudinal membrane residual stresses were $0.055f_y$ in tension and $0.031f_y$ in compression and their low values attributed to the seamless fabrication procedure. Owing to their very low magnitudes compared to the material yield strength, the residual stresses were not explicitly introduced into the FE models. A detailed description of the initial geometric imperfection and residual stress measurements is provided in Wang et al. (2016) and Wang et al. (2017). Residual stress measurements on HSS box sections have also been executed by Rasmussen and Hancock (1995) and Wang et al. (2012). Even though the aforementioned studies have focused on welded sections, in both cases it was concluded that the ratio of the residual stress over the yield strength for HSS sections is lower than the corresponding one of their mild steel counterparts.

2.4. Eccentric stub column tests

To investigate the structural behaviour of HSS hollow sections under combined compression and uniaxial bending, a total of 12 stub columns have been tested under compression with different loading eccentricities to generate different ratios of axial load to bending moment. The average measured geometric dimensions of the test specimens, including the length of the specimen L, the section depth h, the section width b, the thickness t and the average internal corner radius r_i, are reported in Table 4, together with the maximum local geometric imperfection ω_0 and the nominal initial loading eccentricity $e_{0,n}$. In accordance with the technical memorandum B3 (Ziemian, 2010),

the length of the tested specimens was set equal to three times the largest dimension of the cross-section, thus enabling a representative pattern of residual stresses and geometric imperfections to be present in the tested member, while preventing global buckling.

The combined loading tests were conducted in a SATEC 2000 kN hydraulic loading machine. A schematic diagram and a photograph of the test set-up are shown in Figures 3(a) and 3(b) respectively. The specimens were welded onto end-plates at an offset from the centre to include the nominal eccentricities, and then installed into the testing machine by bolting the end-plates to the loading plates. The top and bottom loading plates were in contact with the loading rig through knife edges which provided pin-ended boundary conditions about the axis of bending and fixed-ended boundary conditions about the other axis. In terms of the instrumentation, two LVDTs were placed horizontally at the mid-height of the specimens to measure lateral displacement, thus enabling the second order bending moments, i.e. the bending moments due to the deviation of the mid-section centroid from the line of loading, to be determined. Four strain gauges (two on the concave face and two on the convex face) were attached to each specimen at mid-height to measure the longitudinal strains, which would be used for the determination of the actual calculated initial loading eccentricity, as discussed later. Two inclinometers were attached to the end-plates (one at each end) to record the end-rotation of the specimens. The applied load was obtained from the loading machine. The stub columns were loaded under displacement control at a constant displacement rate of 0.2 mm/min and 0.4 mm/min for the SHS 50×50×5 and SHS 90×90×5.6 specimens respectively. During testing, the load, lateral deflection at mid-height, longitudinal strains and end-rotations were all recorded at one-second intervals using the data acquisition system DATASCAN.

After testing, the strain gauge readings were used to calculate the actual initial loading eccentricities applied to the tested cross-sections, since this has a strong influence on the behaviour of the specimens under combined compression and bending, and is also required for the numerical replication of the tests. Under uniaxial bending and compression, the relationship between the moment M and the axial force N applied to a cross-section is $M = N(e_0 + e')$, where the sum of the initial eccentricity e_0 and the eccentricity generated due to the second order effect e' comprises the

total eccentricity at the mid-height of the specimen. In the initial stages of loading, during which the specimens remain elastic, the theoretical relationships between the applied bending moment and compressive force and the strain gauge readings are given by Equations (1) and (2) respectively, where E is the Young's modulus, I is the second moment of area, A is the area of the cross-section, h is the depth of the cross-section and ε_{convex} and $\varepsilon_{concave}$ are the strains on the convex side and concave side of the cross-section, respectively.

$$M = \frac{EI(\varepsilon_{convex} - \varepsilon_{concave})}{h} \tag{1}$$

$$N = \frac{EA(\varepsilon_{convex} + \varepsilon_{concave})}{2} \tag{2}$$

By substituting the above expressions of M and N into $M = N(e_0 + e')$, the relationship between the strain gauge readings and the initial loading eccentricity e_0 can be established, according to Equation (3), where ψ is the ratio $\varepsilon_{concave}/\varepsilon_{convex}$ and e' is the second order eccentricity recorded by the two lateral LVDTs at the mid-height of the specimen.

$$e_0 = \frac{2I \times (1 - \psi)}{Ah \times (1 + \psi)} - e' \tag{3}$$

All four SHS 90×90×5.6 specimens and the S690 SHS 50×50×5 specimen that was loaded under an eccentricity of 5 mm displayed clear signs of local buckling at failure, as shown in Figures 4(b) and 4(c), while the remaining specimens failed with little visible local buckling, as can be seen in Figure 4(a). The differences in the observed failure mode can be explained by considering the effect of the yield strength and the stress gradient due to the applied loading eccentricity on the cross-section slenderness. For the same cross-section geometry, the S690 sections have a higher yield load but a similar elastic buckling load to their S460 counterparts and are thus more slender and more prone to local buckling occurring prior to yielding. With regards to the stress distribution, the cross-sections with the higher loading eccentricities have a steeper stress gradient in the webs, making the webs less prone to local buckling, which in turn means that they can also provide greater restraint against local buckling to the flanges on the concave side of the cross-section. The load versus end-rotation relationships for all the tested specimens are depicted in Figures 5(a)–5(c), whilst the load versus longitudinal strain curves for typical cases are shown in Figure 6. The key test results are summarised

in Table 5, where N_u is the failure load, e_0 is the calculated initial loading eccentricity based on the strain gauge readings using Equation (3), e_u' is the recorded lateral deflection at the failure load, referred to as the second order eccentricity, M_u is the failure moment given by $M_u = N_u(e_0 + e_u')$ and φ_u is the mean end-rotation at the failure load.

3. Numerical modelling

In parallel with the experimental study, a numerical investigation using the general purpose FE software ABAQUS (Hibbitt et al., 2014) was performed in order to investigate further the structural response of high strength steel hollow sections under combined loading. The finite element models were first validated against the test results and subsequently utilised for the execution of parametric studies, thus generating additional data over a wide range of cross-section slenderness and loading combinations, based upon which design recommendations could be made.

3.1. Modelling assumptions

The four-noded doubly curved shell element S4R with reduced integration and finite membrane strains was adopted for the discretisation of the modelled geometries as it has been shown to perform well in similar studies (Zhao et al., 2015b; Wang et al., 2016). An initial mesh convergence study was performed, resulting in an average element size equal to the material thickness.

The material stress–strain properties were incorporated into the FE models based on the results of the tensile coupon tests, in the form of an elastic-plastic multi linear curve with the von Mises yield criterion and isotropic hardening. Since no significant differences in the stress–strain behaviour between the flat and corner coupon tests or between the tensile and compressive properties were observed, the average values of the material properties obtained from the tensile flat coupon tests, as recorded in Table 3, were utilised for the material model. ABAQUS requires the material properties to be input in the form of a multilinear true stress–logarithmic plastic strain ($\sigma_{true} - \varepsilon_{ln}^{pl}$) curve. Hence, the measured engineering stress–strain curves were converted into the true stress–logarithmic plastic strain curves by means of Equations (4) and (5), where σ_{eng} and ε_{eng} are the engineering stress and

strain respectively, E is the Young's modulus and σ_{true} and ε_{ln}^{pl} are the true stress and logarithmic plastic strain respectively.

$$\sigma_{true} = \sigma_{eng}\left(1 + \varepsilon_{eng}\right) \tag{4}$$

$$\varepsilon_{ln}^{pl} = \ln(1 + \varepsilon_{eng}) - \frac{\sigma_{true}}{E} \tag{5}$$

For modelling convenience and computational efficiency, the effect of the supports and the loading plates was introduced through appropriate boundary conditions and constraints, while only half of the cross-section was modelled, thus exploiting the symmetry with respect to the geometry, boundary conditions, applied load and failure mode of the test specimens. At each end, the degrees of freedom of all nodes were constrained to the degrees of freedom of a control point (CP) node through rigid body constraints, replicating the experimental conditions in which the ends of the specimens were welded to plates, thus preventing any deformation of the end cross-sections. In the initial validation against the experimental data, the top and bottom control points (CPs) were located in a plane perpendicular to the specimen axis and at a distance of 103 mm (equal to the thickness of the knife edges) from the end sections, while in the subsequent parametric studies the CPs were located within the plane of the end sections of the stub columns. The load was applied incrementally as a prescribed displacement at the top control point. All other translational degrees of freedom were restrained at both CPs, whilst all rotational degrees of freedom, except for those allowing flexure due to the eccentrically applied load, were also restrained. The eccentricity of the loading was introduced by offsetting the rigid body control points from the centroid of the section along the symmetry axis. Appropriate symmetry boundary conditions were also applied.

Local geometric imperfections were introduced into the models in the form of the lowest elastic buckling mode shape, in line with previous studies (Gao et al., 2009; Gardner et al., 2011; Zhao et al., 2015b; Wang et al., 2016). In order to investigate the imperfection sensitivity of the models, five values of local imperfection amplitude were examined: 1%, 2% and 10% of the section wall thickness, the maximum measured imperfection ω_0 as given in Table 4 and an imperfection amplitude (ω_{DW}) based on the predictive model developed by Dawson and Walker (Dawson and Walker, 1972;

Gardner and Nethercot, 2004), as defined by Equation (6), where f_y is the yield strength of the plate

material and σ_{cr} is the elastic buckling stress of the most slender plate in the cross-section, which is a

function of its width-to-thickness ratio.

$$\omega_{DW} = \beta \left(\frac{f_y}{\sigma_{cr}} \right)^{0.5} t \tag{6}$$

The coefficient β can be determined through regression analysis of measured imperfection data, but

due to the limited available imperfection data for HSS sections, the value of $\beta = 0.028$, as proposed in

Gardner et al. (2010) for normal strength carbon steel hot-finished SHS and RHS, was adopted.

Owing to their very low magnitude (see Section 2.3), it was decided not to explicitly incorporate

residual stresses into the numerical models. A nonlinear static analysis, accounting for both material

and geometric nonlinearities, using the modified Riks procedure (Hibbitt et al., 2014) was performed

in order to trace the full load–deformation response path of the modelled specimens.

3.2. Validation of the FE model

Utilising the modelling assumptions described above, the response of the tested specimens was

simulated for the purposes of model validation. Typical comparisons between the test and FE load

versus end-rotation curves for S460 and S690 specimens are shown in Figures 7(a) and 7(b),

respectively. As can be observed, the initial stiffness and the overall structural response are accurately

captured. As anticipated, for the more stocky S460 section shown in Figure 7(a), which failed without

noticeable local deformation, variation in the initial local imperfection amplitude does not have

significant influence on the observed response, whereas for the more slender S690 section shown in

Figure 7(b), which displayed clear evidence of local buckling, the sensitivity to the local geometric

imperfection amplitude is more pronounced. The failure modes were accurately captured in all cases,

as indicated by the typical comparisons shown in Figures 8(a) and 8(b).

For all specimens, the ratios of the numerical-to-experimental ultimate loads ($N_{u,FE}/N_{u,exp}$) and

moments ($M_{u,FE}/M_{u,exp}$) for the different considered imperfection amplitudes are summarised in

Table 6. It can be concluded that, overall, very good agreement between the experimental and

numerical results has been achieved, with the FE predictions being slightly on the conservative side in most cases. The best agreement was obtained when the measured imperfection amplitudes ω_0 were employed in the FE models, with a mean value of $N_{u,FE}/N_{u,exp}$ equal to 0.92 and a mean value of $M_{u,FE}/M_{u,exp}$ equal to 0.98. However, very similar results were also achieved when an initial geometric imperfection amplitude of $t/50$ was employed; this imperfection amplitude was therefore adopted in the subsequent parametric study, described in Section 3.3.

3.3. Parametric study

Upon successful validation of the FE models against the test results, an extensive parametric study was performed in order to generate data over a wide range of cross-section slendernesses and initial loading eccentricities corresponding to different ratios of axial load to bending moments. The average material properties of the tensile flat coupon tests were incorporated in the models, whereas an initial local geometric imperfection amplitude of $t/50$, which gave the closest agreement with the test results, was used in all numerical models. Similar to the experiments, the length of the modelled stub columns was set to be three times the largest cross-sectional dimension, while the internal radius was set equal to half the cross-sectional thickness.

The loading eccentricities applied to the modelled stub columns were varied to generate a range of initial stress ratios ψ over the cross-section depth from -0.75 to 1.00; the stress ratio ψ was defined, as in EN 1993-1-5 (2006), as the ratio of the stress on the most heavily compressed side of the cross-section to that on the least heavily compressed (or most tensioned) side, assuming elastic material behaviour, with ψ = 1.00 corresponding to pure compression and ψ = -1.00 corresponding to pure bending.

Three cross-section aspect ratios (h/b) of 1.00, 2.00 and 2.44, with varying thickness, were considered. The cross-section slenderness was taken as the *c/tε* ratio of the most slender plate element in accordance with the current cross-section classification practice adopted in EN 1993-1-1 (2014). The cross-section aspect ratio of 2.44 represents the case where the web and the flange of an RHS subjected to pure bending about the major axis, allowing for their respective stress distributions, are of

the same non-dimensional plate slenderness $\bar{\lambda}_p$, as defined in EN 1993-1-5 (2006) (Wang et al., 2016).

The cases of both compression plus major axis bending and compression plus minor axis bending were considered in the parametric study. In total, 720 analyses of eccentrically loaded stub columns were performed using the validated finite element models. Typical elastic buckling mode shapes and failure modes of the eccentrically loaded stub column FE models are depicted in Figures 9(a) and 9(b) respectively. The ultimate load bearing capacity N_u and the corresponding moment at mid-height accounting for second order effects M_u were determined for each analysis, while the full moment versus end-rotation responses for some typical cases are shown in Figures 10(a) and 10(b). The results of the experiments and the FE parametric study are analysed and used to assess the European design provisions in the following section.

4. Analysis of the results and design recommendations

4.1. Introduction

Based on the obtained test and FE results, the Eurocode N-M interaction curves for HSS SHS and RHS (EN 1993-1-1, 2014) are assessed in this section. The test and FE results are compared with the corresponding codified N-M interaction curves in Figures 11–13 for Class 1 and 2, Class 3 and Class 4 cross-sections, respectively. In the figures, the axial compressive force at failure and the second order bending moment at failure have been normalised by their respective resistances according to the cross-section class. Depending on the cross-section properties and the applied loading conditions, each specimen was classified in accordance with Table 5.2 of EN 1993-1-1 (2014).

The comparisons between the test/FE results and the Eurocode design predictions are presented numerically in Table 7 for all cross-sections. The assessment is based on the utilisation ratio of the test or FE to the predicted capacity (R_{exp}/R_{pred} or R_{FE}/R_{pred}), which is graphically defined in Figure 14.

4.2. Assessment of the Eurocode interaction curve for Class 1 and 2 cross-sections

The interaction curves for determining the resistance of Class 1 and Class 2 cross-sections under combined axial load and bending are provided in Clause 6.2.9.1(5) in EN 1993-1-1 (2014), and are presented in Equations (7) and (8) for major axis and minor axis bending respectively.

$$M_{N,y,Rd} = M_{pl,y,Rd}(1 - n)/(1 - 0.5a_w) \text{ but } M_{N,y,Rd} \leq M_{pl,y,Rd} \tag{7}$$

$$M_{N,z,Rd} = M_{pl,z,Rd}(1 - n)/(1 - 0.5a_f) \text{ but } M_{N,z,Rd} \leq M_{pl,z,Rd}, \tag{8}$$

where $n = N_{Ed}/N_{pl,Rd}$, N_{Ed} is the design axial compressive load, $N_{pl,Rd}$ is the cross-section yield load (Af_y), $M_{N,Rd}$ is the reduced cross-section moment resistance to allow for the presence of axial load, $M_{pl,Rd}$ is the cross-section plastic moment capacity $(W_{pl}f_y)$, $a_w = (A - 2bt_w)/A$ but $a_w \leq 0.5$ and $a_f = (A - 2bt_f)/A$ but $a_f \leq 0.5$. The subscripts y and z in Equations (7) and (8) denote the major and minor axis, respectively.

The codified N-M curves are compared with the test and FE results obtained for the Class 1 and 2 (i.e. those that can develop their full plastic moment capacity) SHS and RHS in compression plus major axis bending (Figure 11(a)), and RHS in compression plus minor axis bending (Figure 11 (b)). The test and FE results may be seen to generally follow the trend of the Eurocode 3 interaction equation, though predictions are very conservative in the case of the stocky cross-sections (low c/tε ratios), particularly for the S460 steel. This conservatism stems principally from the neglect of strain hardening in the Eurocode interaction equations, and is therefore most pronounced for those cross-sections that are most resistant to local buckling (i.e. low local slenderness) and hence have high deformation capacity and for material that exhibits a high degree of strain hardening, which is more prominent in lower strength steel grades. It should be noted that at the high bending moment end of the interaction curves, some of the S690 tests and FE results fall marginally below M_{pl}. This was also observed by Wang et al. (2016), and again, attributed principally to the lower degree of strain hardening that the higher grades of steel exhibit. For the S460 RHS specimens under compression and minor axis bending, there is an apparent change in the response of the stockier (i.e. lower c/tε)

specimens at the higher axial load levels (see Figure 11(b)). In fact, the response of the specimens does not change significantly, but the value of the second order moment at failure M_u is sensitive to where the peak load arises on the rather flat load–lateral deflection curves. Overall, the graphical comparisons indicate that the existing interaction curves are generally applicable to high strength steel material, and similar conclusions are reached from the numerical comparisons presented in Table 7.

4.3. Assessment of the Eurocode interaction curve for Class 3 cross-sections

The linear N-M interaction expression for Class 3 cross-sections specified in EN 1993-1-1 (2014) is given by Equation (9).

$$\frac{N_{Ed}}{N_{Rd}} + \frac{M_{y,Ed}}{M_{el,y,Rd}} + \frac{M_{z,Ed}}{M_{el,z,Rd}} \leq 1 \tag{9}$$

where $M_{el,Rd}$ is the elastic moment capacity ($W_{el}f_y$) of the cross-section and all other symbols are as previously defined.

The FE results for Class 3 cross-sections are compared against the Eurocode 3 linear interaction N-M equation in Figure 12. The interaction equation may be seen to yield generally safe side predictions and without excessive conservatism (R_{FE}/R_{pred}=1.15), but improved predictions and reduced scatter are achieved using the linear transition (see Figure 15) between the M_{el} and M_{pl} for Class 3 cross-sections (R_{FE}/R_{pred}=1.09) proposed by Taras et al. (2013); the application of this proposal to HSS is therefore supported in the present paper.

4.4. Assessment of the effective width equations for Class 4 cross-sections

For Class 4 cross-sections under combined axial load and bending, the linear N-M interaction expression given by Equation (10) is provided in EN 1993-1-1 (2014).

$$\frac{N_{Ed}}{A_{eff}f_y} + \frac{M_{y,Ed} + N_{Ed}e_{Ny}}{W_{eff,y,min}f_y} + \frac{M_{z,Ed} + N_{Ed}e_{Nz}}{W_{eff,z,min}f_y} \leq 1 \tag{10}$$

where A_{eff} is the effective area of the cross-section when subjected to uniform compression, $W_{eff,min}$ is the effective section modulus (corresponding to the fibre with the maximum elastic stress)

of the cross-section when subjected only to bending about the relevant axis, and e_N is the shift in the relevant neutral axis of the effective cross-section under pure compression (which is zero for doubly symmetric sections as examined herein); all other parameters are as previously defined.

The FE results for Class 4 cross-sections are compared against the Eurocode 3 linear interaction N-M equation in Figure 13, where the data points have been normalised based on their respective effective section properties calculated according to EN 1993-1-5 (2006). The results shown in Figure 13 closely follow the design predictions, indicating that both the effective section properties and interaction curve are appropriate for HSS.

5. Conclusions

A comprehensive study into the structural behaviour of hot-rolled high strength steel (S460 and S690) hollow sections under compression and uniaxial bending has been reported. Upon the execution of twelve tests on eccentrically loaded stub columns, together with complementary measurements of geometric and material properties, an extensive numerical programme was conducted in order to generate additional data over a wide range of cross-section slendernesses and loading eccentricities, generating different proportions of axial compression and bending moment at failure. The results have been utilised for the assessment of the design provisions specified in EN 1993-1-1 (2014) for cross-sections under combined compression and uniaxial bending moment. The Eurocode interaction curve for Class 1 and 2 sections generally provides safe side predictions, but was found to be rather conservative for the stockier cross-sections and lower steel grade. The linear interaction curve for Class 3 sections gives accurate, though again slightly conservative design predictions, while the use of a linear transition between M_{el} and M_{pl}, as proposed by Taras et al. (2013), reduced this conservatism. The effective width equations were shown to be generally applicable to S460 and S690 square and rectangular hollow sections subjected to compression and uniaxial bending. Overall the design provisions of EN 1993-1-1 (2014) are deemed suitable for high strength steel sections.

References

AISI S100 (2012) North American specification for the design of cold-formed steel structural members. Washington DC, USA. American Iron and Steel Institute Standards.

ANSI/AISC 360-10 (2010) Specification for structural steel buildings. Chicago, Illinois. American Institute of Steel Construction.

Arrayago I and Real E (2015) Experimental study on ferritic stainless steel RHS and SHS cross-sectional resistance under combined loading. Structures 4: 69–79. Elsevier.

AS 4100-A1 (2012) Amendment no.1 to AS 4100–1998 steel structures. Sydney, Australia. Australian Standard.

Ban H, Shi G, Shi Y and Bradford MA (2013) Experimental investigation of the overall buckling behaviour of 960 MPa high strength steel columns. Journal of Constructional Steel Research 88: 256–266.

Beg D and Hladnik L (1996) Slenderness limit of Class 3 I cross-sections made of high strength steel. Journal of Constructional Steel Research 38(3): 201–217.

Bjorhovde R (2004) Development and use of high performance steel. Journal of Constructional Steel Research 60(3): 393–400.

CAN/CSA-S16-01 (2001) Limit states design of steel structures. Rexdale, Ontario, Canada. Canadian Standard Association.

Dawson RG and Walker AC (1972) Post-buckling of geometrically imperfect plates. Journal of the Structural Division 98(1): 75–94.

EN 1993-1-1: 2005 +A1 (2014) Eurocode 3: Design of steel structures. Part 1-1: General rules and rules for buildings. Brussels, Belgium. European Committee for Standardization (CEN).

EN 1993-1-12 (2007) Eurocode 3: Design of steel structures. Part 1-12: Additional rules for the extension of EN 1993 up to steel grades S 700. Brussels, Belgium. European Committee for Standardization (CEN).

EN 1993-1-5 (2006) Eurocode 3: Design of steel structures. Part 1-5: Plated structural elements. Brussels, Belgium. European Committee for Standardization (CEN).

Fujimoto T, Mukai A, Nishiyama I and Sakino K (2004) Behavior of eccentrically loaded concrete-filled steel tubular columns. Journal of Structural Engineering 130(2): 203–212.

Gao L, Sun H, Jin F and Fan H (2009) Load-carrying capacity of high-strength steel box-sections I: Stub columns. Journal of Constructional Steel Research 65(4): 918–924.

Gardner L and Nethercot DA (2004) Numerical modeling of stainless steel structural components - A consistent approach. Journal of Structural Engineering 130(10): 1586–1601.

Gardner L, Chan TM and Abela JM (2011) Structural behaviour of elliptical hollow sections under combined compression and uniaxial bending. Advanced Steel Construction 7(1): 86–113.

Gardner L, Saari N and Wang F (2010) Comparative experimental study of hot-rolled and cold-formed rectangular hollow sections. Thin-Walled Structures 48(7): 495–507.

GB 50017-2003 (2006) Code for design of steel structures. China Architecture & Building Press. Beijing, China. In Chinese.

Gkantou M, Antoniou N, Theofanous M and Baniotopoulos C (accepted) Compressive behaviour of high strength steel cross-sections. Proceedings of the Institution of Civil Engineers.

Hibbitt, Karlsson and Sorensen Inc ABAQUS (2014) ABAQUS/Standard user's manual volume IIII and ABAQUS CAE manual. Version 6.14. Pawtucket, USA.

Höglund T, Collin P, Müller C, Schröter F and Miazzon A (2005) Chapter 5.5 – Examples and applications. In use and application of high-performance steels for steel structures. International Association for Bridge and Structural Engineering (IABSE).

ISO 6892-1 (2009) British Standard: Metallic materials - Tensile testing. Part 1: Method of test at ambient temperature. The Standards Policy and Strategy Committee.

Kim DK, Lee CH, Han KH, Kim JH, Lee SE and Sim HB (2014) Strength and residual stress evaluation of stub columns fabricated from 800 MPa high-strength steel. Journal of Constructional Steel Research 102: 111–120.

Lee CH, Han KH, Uang CM, Kim DK, Park CH and Kim JH (2012) Flexural strength and rotation capacity of I-shaped beams fabricated from 800-MPa steel. Journal of Structural Engineering 139(6): 1043–1058.

McDermott JF (1969) Plastic bending of A514 steel beams. Journal of the Structural Division 95(9): 1851–1871.

Rasmussen KJR and Hancock GJ (1992) Plate slenderness limits for high strength steel sections. Journal of Constructional Steel Research 23(1): 73–96.

Rasmussen KJR and Hancock GJ (1995) Test of high strength steel columns. Journal of Constructional Steel Research 34(1): 27–52.

Ricles JM, Sause R and Green PS (1998) High-strength steel: implications of material and geometric characteristics on inelastic flexural behavior. Engineering Structures 20(4): 323–335.

Sheehan T, Dai XH, Chan TM and Lam D (2012) Structural response of concrete-filled elliptical steel hollow sections under eccentric compression. Engineering Structures 45: 314–323.

Shi G, Ban H and Bijlaard FS (2012) Tests and numerical study of ultra-high strength steel columns with end restraints. Journal of Constructional Steel Research 70: 236–247.

Shi G, Zhou W, Bai Y and Lin C (2014) Local buckling of 460 MPa high strength steel welded section stub columns under axial compression. Journal of Constructional Steel Research 100: 60–70.

Taras A, Greiner R and Unterweger H (2013) Proposal for amended rules for member buckling and semi-compact cross-section design. Technical Report. Consolidated Version of Documents of the Same Title Submitted to the SC3 Evolution Group 1993–1–1. Paris.

Usami T and Fukumoto Y (1984) Welded box compression members. Journal of Structural Engineering 110(10): 2457–2470.

Wang J, Afshan S, Gkantou M, Theofanous M, Baniotopoulos C and Gardner L (2016) Flexural behaviour of hot-finished high strength steel square and rectangular hollow sections. Journal of Constructional Steel Research 121: 97–109.

Wang J, Afshan S, Schillo N, Theofanous M, Feldmann M and Gardner L (2017) Material properties and compressive local buckling response of high strength steel square and rectangular hollow sections. Engineering Structures 130: 297–315.

Wang YB, Li GQ and Chen SW (2012) The assessment of residual stresses in welded high strength steel box sections. Journal of Constructional Steel Research 76: 93–99.

Wang YB, Li GQ, Chen SW and Sun FF (2014) Experimental and numerical study on the behaviour of axially compressed high strength steel box-columns. Engineering Structures 58: 79–91.

Yang D and Hancock GJ (2004) Compression tests of cold-reduced high strength steel sections. I: stub columns. Journal of Structural Engineering 130(11): 1772–1781.

Yang D and Hancock GJ (2006) Numerical simulation of high-strength steel box-shaped columns failing in local and overall buckling modes. Journal of Structural Engineering 132(4): 541–549.

Yang D, Hancock GJ and Rasmussen KJ (2004) Compression tests of cold-reduced high strength steel sections. II: long columns. Journal of Structural Engineering 130(11): 1782–1789.

Yoo JH, Kim JW, Yang JG, Kang JW and Lee MJ (2013) Local buckling in the stub columns fabricated with HSA800 of high performance steel. International Journal of Steel Structures 13(3): 445–458.

Zhao O, Rossi B, Gardner L and Young B (2015a) Behaviour of structural stainless steel cross-sections under combined loading – Part I: Experimental study. Engineering Structures 89: 236–246.

Zhao O, Rossi B, Gardner L and Young B (2015b) Behaviour of structural stainless steel cross-sections under combined loading – Part II: Numerical modelling and design approach. Engineering Structures 89: 247–259.

Ziemian RD (2010) Guide to stability design criteria for metal structures. 6th ed. New York. John Wiley & Sons.

Figure 8: Comparison between typical experimental and numerical failure modes: a) S460 SHS 50×50×5 (e_0=20.22 mm), b) S690 SHS 90×90×5.6 (e_0=5.37 mm)

Figure 9: Typical numerical elastic buckling and failure modes for eccentrically loaded stub column: a) Elastic buckling modes, b) Failure modes

Figure 10: Typical numerical moment versus end-rotation curves: a) S460 SHS, $c/t\varepsilon$=50

b) S460 SHS, ψ=-0.50

Figure 11: Assessment of N-M interaction curves for Class 1 and 2 cross-sections: a) SHS and RHS bending about the major axis, b) RHS bending about the minor axis

Figure 12: Assessment of N-M interaction curve for Class 3 cross-sections

Figure 13: Assessment of effective section properties and interaction curves for Class 4 cross-sections

Figure 14: Definition of utilisation ratio of the test or FE to predicted capacities

Figure 15: Bending resistances for different cross-section classes, including illustration of linear transition for Class 3 cross-sections (after Taras et al., 2013)

Table 1: Chemical composition of tested specimens

Cross-section	C (%)	Si (%)	Mn (%)	P (‰)	S (‰)	Cu (%)	Cr (%)	Ni (%)	Mo (%)	V (%)	Ti (‰)	Nb (‰)	B (‰)	Al (‰)
S460 SHS 50×50×5	0.15	0.37	1.53	0.17	0.01	0.02	0.07	0.06	0.03	0.10	0.03	0.01	-	-
S690 SHS 50×50×5	0.15	0.28	1.50	0.10	0.02	0.02	0.67	0.12	0.21	0.07	0.04	0.31	0.003	0.30
S690 SHS 90×90×5.6	0.15	0.29	1.53	0.10	0.01	0.04	0.69	0.10	0.21	0.06	0.04	0.27	0.003	0.21

Table 2: Mechanical properties as stated in mill certificates

Cross-section	$f_{y,mill}$ (N/mm^2)	$f_{u,mill}$ (N/mm^2)	ε_f (%)
S460 SHS 50×50×5	473	615	26.5
S690 SHS 50×50×5	797	838	22.4
S690 SHS 90×90×5.6	789	825	16.6

Table 3: Average measured material properties from coupon tests

Cross-section	Label	E (N/mm^2)	f_y (N/mm^2)	f_u (N/mm^2)	ε_u (%)	ε_f (%)	f_u/f_y
S460 SHS 50×50×5	TF	211100	505	620	14.9	31.0	1.23
	TC	208000	481	631	12.7	26.0	1.31
	CF	219000	505	-	-	-	-
S690 SHS 50×50×5	TF	204200	759	790	7.5	21.7	1.04
	TC	209000	782	813	6.9	18.0	1.04
	CF	220000	813	-	-	-	-
S690 SHS 90×90×5.6	TF	205700	774	790	7.4	20.1	1.02
	TC	224000	754	784	9.0	18.0	1.04
	CF	215000	798	-	-	-	-

Table 4: Mean measured dimensions of eccentric stub column specimens

Cross-section	$e_{0,n}$ (mm)	L (mm)	h (mm)	b (mm)	t (mm)	r_i (mm)	ω_0 (mm)
S460 SHS 50×50×5	5	149.98	50.03	49.86	4.94	3.00	0.054
	10	150.01	49.86	50.16	4.98	3.00	0.054
	20	149.95	50.32	50.11	4.90	3.00	0.054
	30	149.97	50.07	50.36	4.95	3.00	0.054
S690 SHS 50×50×5	5	149.91	50.24	50.60	5.03	3.00	0.076
	10	149.96	50.27	50.39	4.94	3.00	0.076
	15	149.84	50.45	50.52	4.96	3.00	0.076
	20	149.98	50.16	50.36	4.97	3.00	0.076
S690 SHS 90×90×5.6	5	269.07	89.56	89.81	5.68	4.50	0.089
	10	269.00	89.84	90.10	5.65	4.63	0.089
	25	268.96	90.21	90.65	5.72	4.88	0.089
	30	269.02	90.57	90.08	5.59	4.63	0.089

Table 5: Key results for eccentric stub column tests

Cross-section	e_0 (mm)	N_u (kN)	e_u' (mm)	M_u (kNm)	φ_u (°)
S460 SHS 50×50×5	4.83	333.8	8.70	4.5	6.98
	9.70	297.3	9.28	5.7	7.62
	20.22	226.6	8.72	6.6	7.19
	33.02	181.4	10.32	7.9	8.39
S690 SHS 50×50×5	5.58	530.8	1.12	3.6	1.02
	10.26	459.5	0.98	5.3	1.80
	13.65	398.7	1.67	6.0	2.25
	19.32	338.2	6.34	8.7	5.20
S690 SHS 90×90×5.6	5.37	1289.5	0.61	7.6	0.46
	10.25	1195.3	0.55	12.9	0.62
	25.49	864.0	3.12	24.9	2.04
	29.80	819.6	2.12	26.2	4.85

Table 6: Comparison of numerical and experimental results for the different considered imperfection amplitudes

Cross-section	$e_{0,n}$ (mm)	ω_0 $\frac{N_{u,FE}}{N_{u,exp}}$	ω_0 $\frac{M_{u,FE}}{M_{u,exp}}$	ω_{DW} $\frac{N_{u,FE}}{N_{u,exp}}$	ω_{DW} $\frac{M_{u,FE}}{M_{u,exp}}$	$t/100$ $\frac{N_{u,FE}}{N_{u,exp}}$	$t/100$ $\frac{M_{u,FE}}{M_{u,exp}}$	$t/50$ $\frac{N_{u,FE}}{N_{u,exp}}$	$t/50$ $\frac{M_{u,FE}}{M_{u,exp}}$	$t/10$ $\frac{N_{u,FE}}{N_{u,exp}}$	$t/10$ $\frac{M_{u,FE}}{M_{u,exp}}$
S460 SHS 50×50×5	5	0.92	0.93	0.92	0.93	0.92	0.93	0.93	0.94	0.94	0.96
	10	0.91	0.93	0.91	0.92	0.91	0.93	0.91	0.93	0.90	0.53
	20	0.92	0.95	0.92	0.95	0.92	0.95	0.91	0.95	0.91	0.92
	30	0.87	0.86	0.87	0.86	0.87	0.86	0.87	0.86	0.86	0.85
S690 SHS 50×50×5	5	0.94	0.95	0.94	0.95	0.94	0.95	0.94	0.95	0.95	0.95
	10	0.89	0.97	0.89	0.97	0.89	0.97	0.89	0.97	0.89	0.96
	15	0.93	1.01	0.93	1.01	0.93	1.01	0.93	1.01	0.93	1.01
	20	0.94	0.84	0.94	0.84	0.94	0.84	0.94	0.84	0.94	0.84
S690 SHS 90×90×5.6	5	0.93	1.01	0.93	1.01	0.93	1.01	0.93	1.01	0.92	0.97
	10	0.89	1.00	0.89	1.00	0.89	1.00	0.89	1.00	0.89	0.97
	25	0.96	1.09	0.96	1.12	0.96	1.12	0.96	1.09	0.95	0.94
	30	0.94	1.21	0.94	1.23	0.94	1.23	0.94	1.21	0.93	1.06
Mean		0.92	0.98	0.92	0.98	0.92	0.98	0.92	0.98	0.92	0.91
COV		0.03	0.10	0.03	0.11	0.03	0.11	0.03	0.10	0.03	0.15

Table 7: Assessment of Eurocode design predictions based on utilisation ratios of the test or FE to the predicted capacities

Cross-section	Aspect ratio	Bending axis	No. of test or FE results	R_{exp}/R_{pred} or R_{FE}/R_{pred}			
				Classes 1 and 2	Class 3	Class 3 (linear transition)	Class 4
S460 SHS-test	1.00	N/A	4	1.29	N/A	N/A	N/A
S690 SHS-test	1.00	N/A	8	1.07	N/A	N/A	N/A
S460 SHS-FE	1.00	N/A	72	1.11	1.11	1.07	1.11
S690 SHS-FE	1.00	N/A	72	1.05	1.11	1.07	1.10
S460 RHS-FE	2.00	major	72	1.16	1.19	1.13	1.10
S690 RHS-FE	2.00	major	72	1.07	1.19	1.12	1.08
S460 RHS-FE	2.00	minor	72	1.05	1.08	1.05	1.12
S690 RHS-FE	2.00	minor	72	1.02	1.08	1.05	1.11
S460 RHS-FE	2.44	major	72	1.10	1.23	1.13	1.10
S690 RHS-FE	2.44	major	72	1.03	1.23	1.13	1.09
S460 RHS-FE	2.44	minor	72	1.03	1.09	1.05	1.16
S690 RHS-FE	2.44	minor	72	1.02	1.09	1.05	1.13
Mean				1.05	1.15	1.09	1.10
COV				0.09	0.07	0.05	0.04
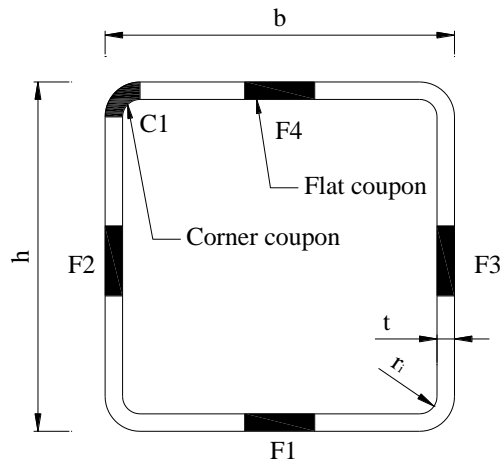
Figure 1: Locations of tensile flat and tensile corner coupons and definition of cross-section symbols
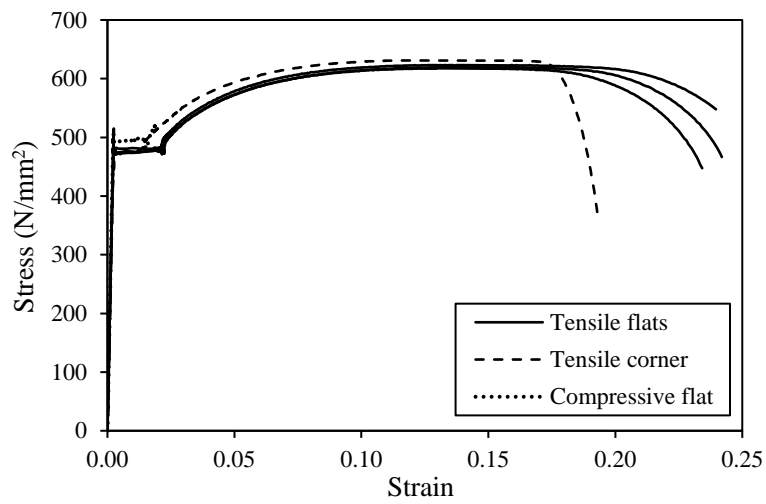
a) S460 SHS 50×50×5
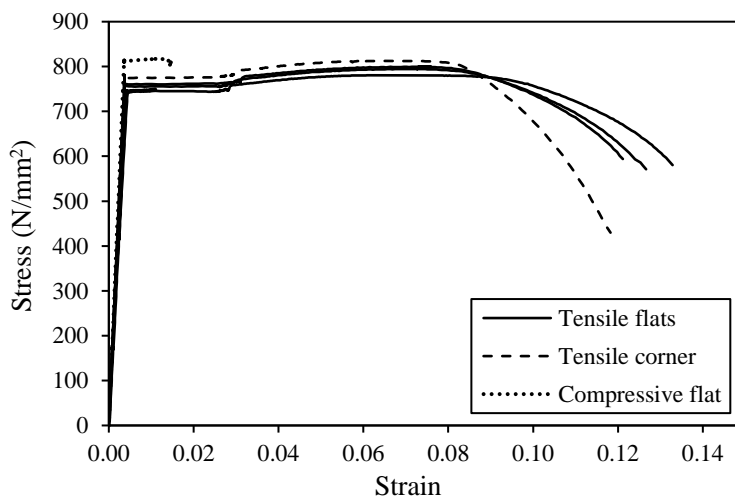
b) S690 SHS 50×50×5

Figure 2: Measured stress–strain curves for tensile flat, tensile corner and compressive flat coupons
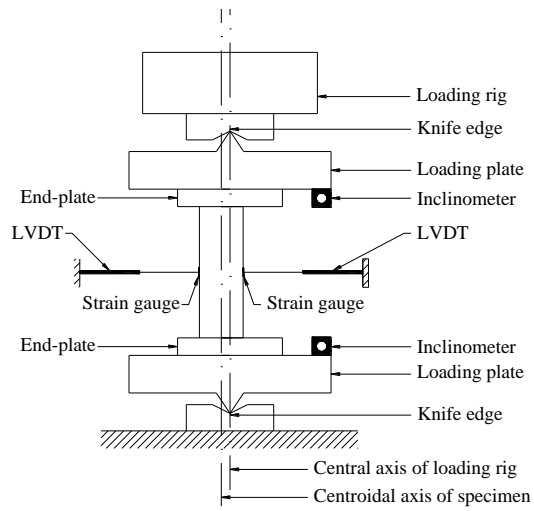
a) Schematic diagram of test set-up   b) Photograph of test set-up

Figure 3: Experimental set-up including instrumentation

a) S460 SHS $50 \times 50 \times 5$ (e_0=20.22 mm)

b) S690 SHS $50 \times 50 \times 5$ (e_0=5.58 mm)

c) S690 SHS $90 \times 90 \times 5.6$ (e_0=5.37 mm)

Figure 4: Failure modes of eccentrically loaded stub columns
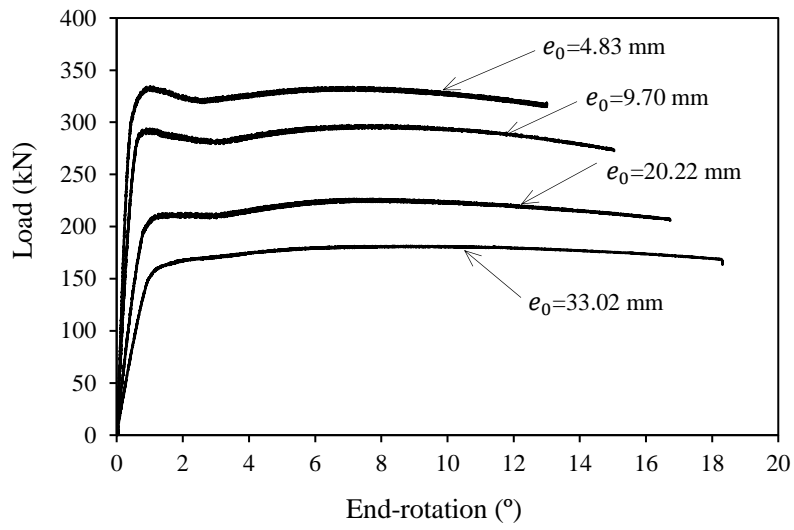
a) S460 SHS 50×50×5
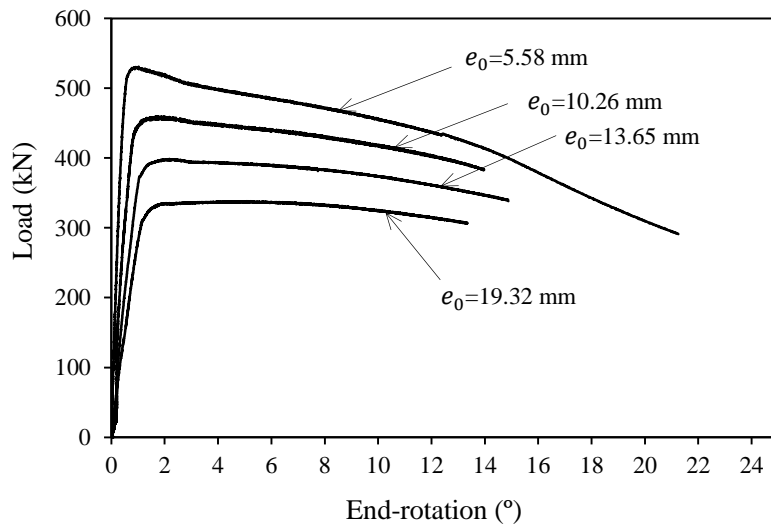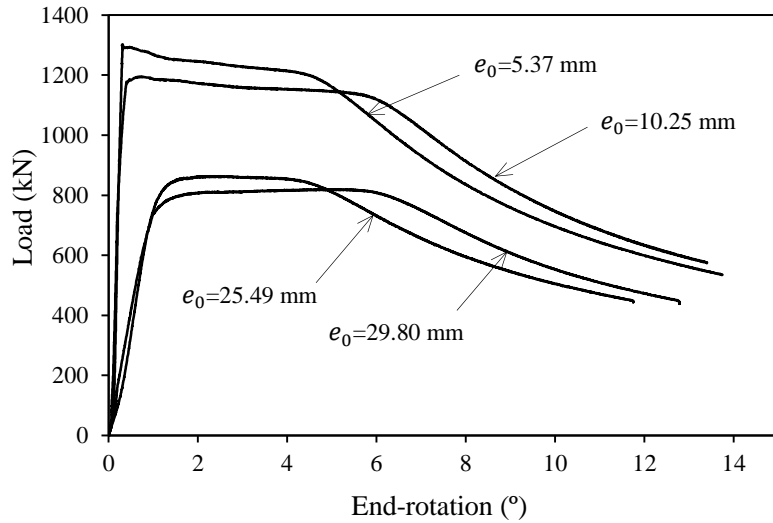
b) S690 SHS 50×50×5

c)   S690 SHS 90×90×5.6

Figure 5: Load versus end-rotation curves from eccentrically loaded stub column tests
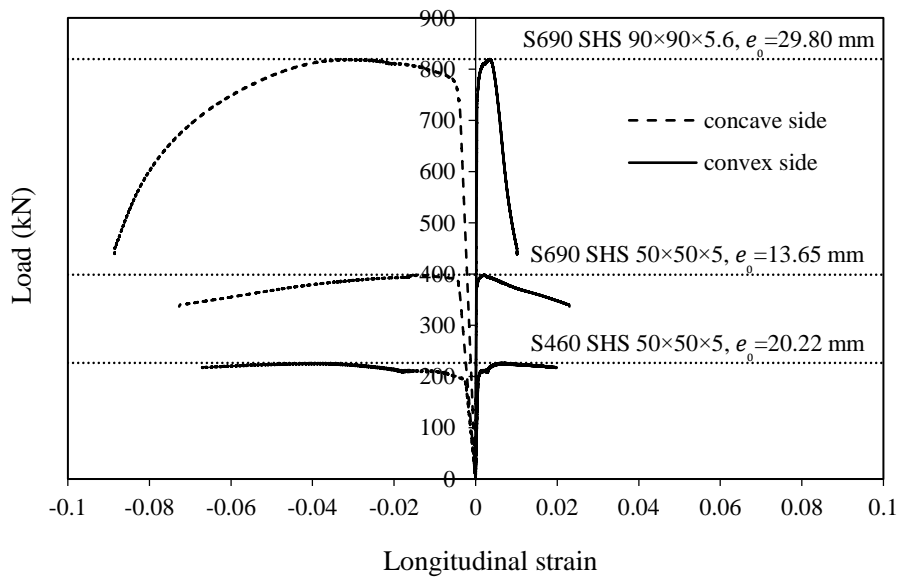
Figure 6: Typical load versus longitudinal strain curves from eccentrically loaded stub column tests
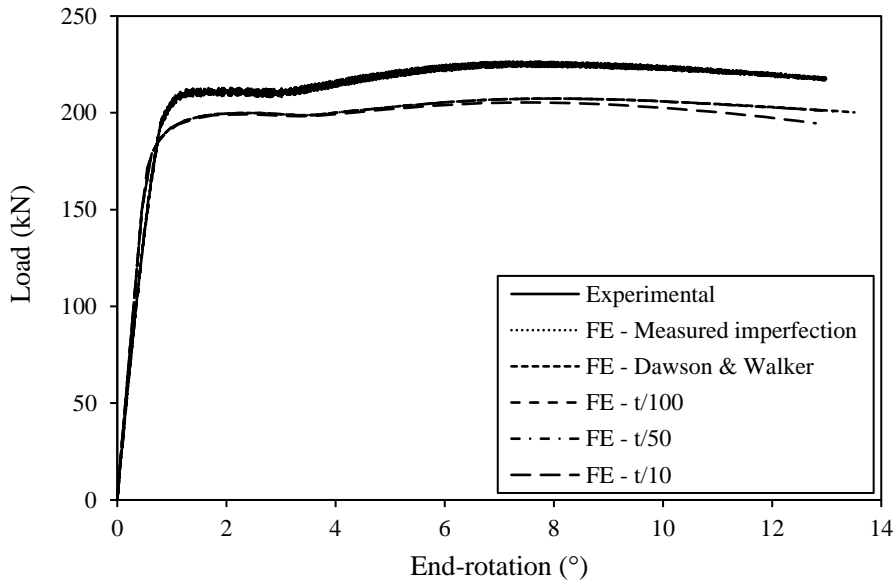
a) S460 SHS 50×50×5 (e_0=20.22 mm)
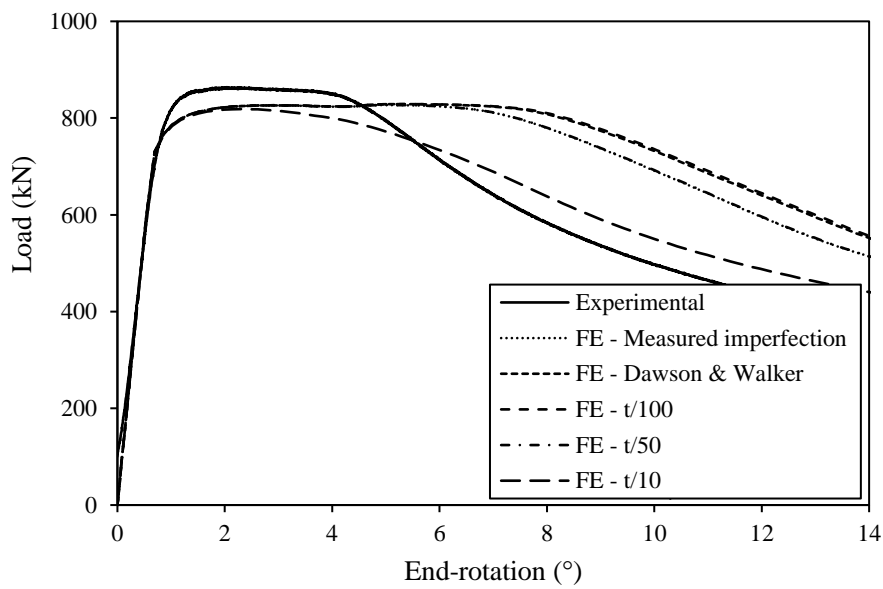
b) S690 SHS 90×90×5.6 (e_0=25.49 mm)

Figure 7: Comparison between typical experimental and numerical load versus end-rotation curves
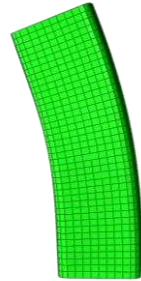
a) S460 SHS 50×50×5 (e_0=20.22 mm)
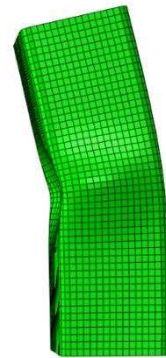
b) S690 SHS 90×90×5.6 (e_0=5.37 mm)

Figure 8: Comparison between typical experimental and numerical failure modes
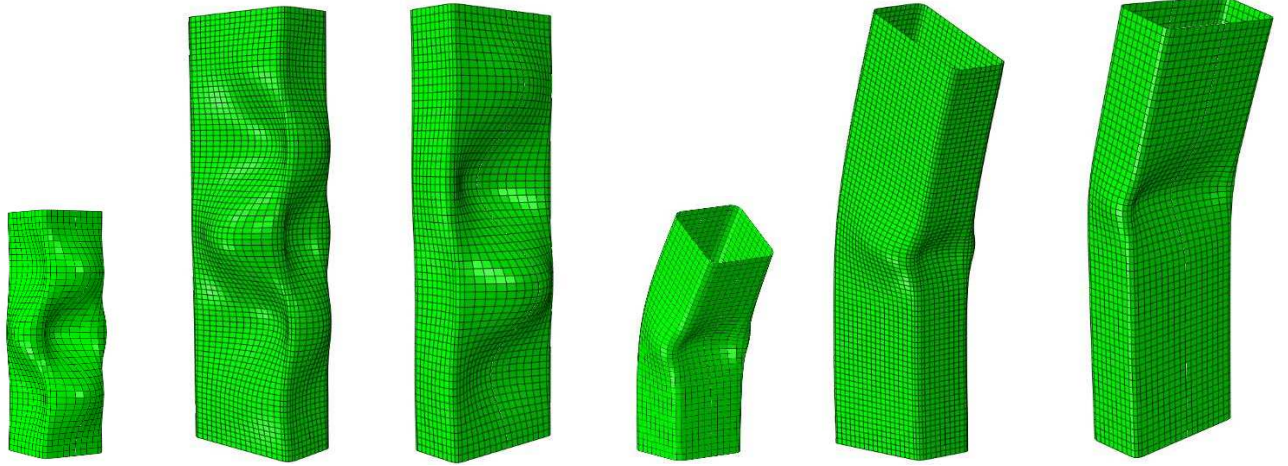
a) Elastic buckling modes   b) Failure modes

Figure 9: Typical numerical elastic buckling and failure modes for eccentrically loaded stub column

models
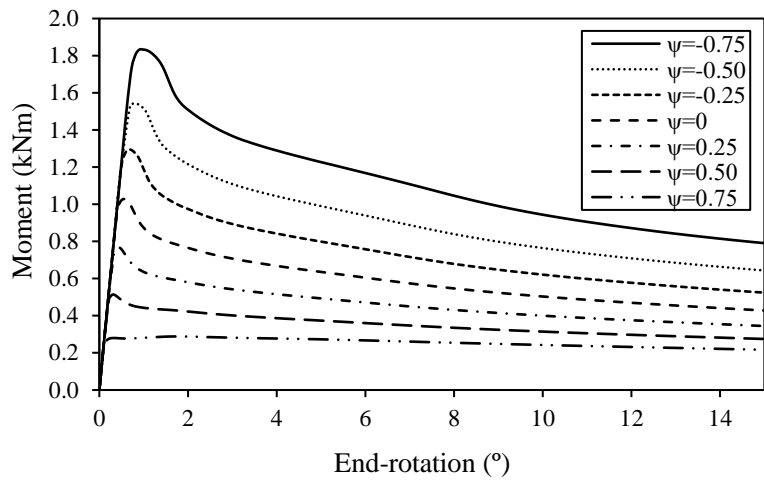
a) S460 SHS, $c/t\varepsilon$=50
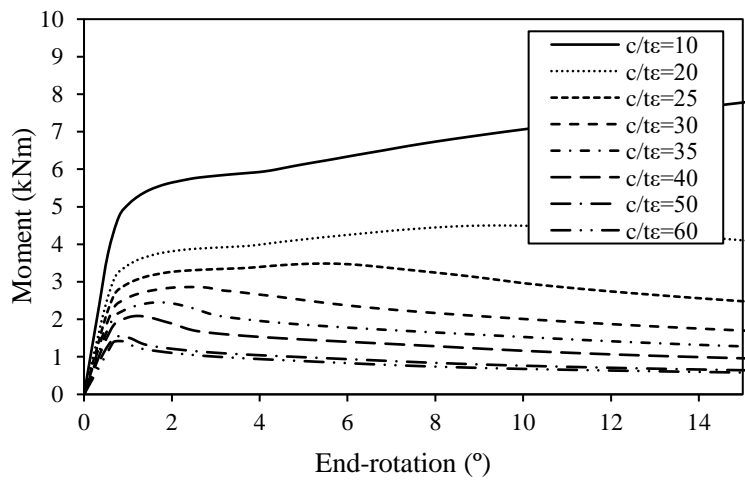
b) S460 SHS, ψ=-0.50

Figure 10: Typical numerical moment versus end-rotation curves
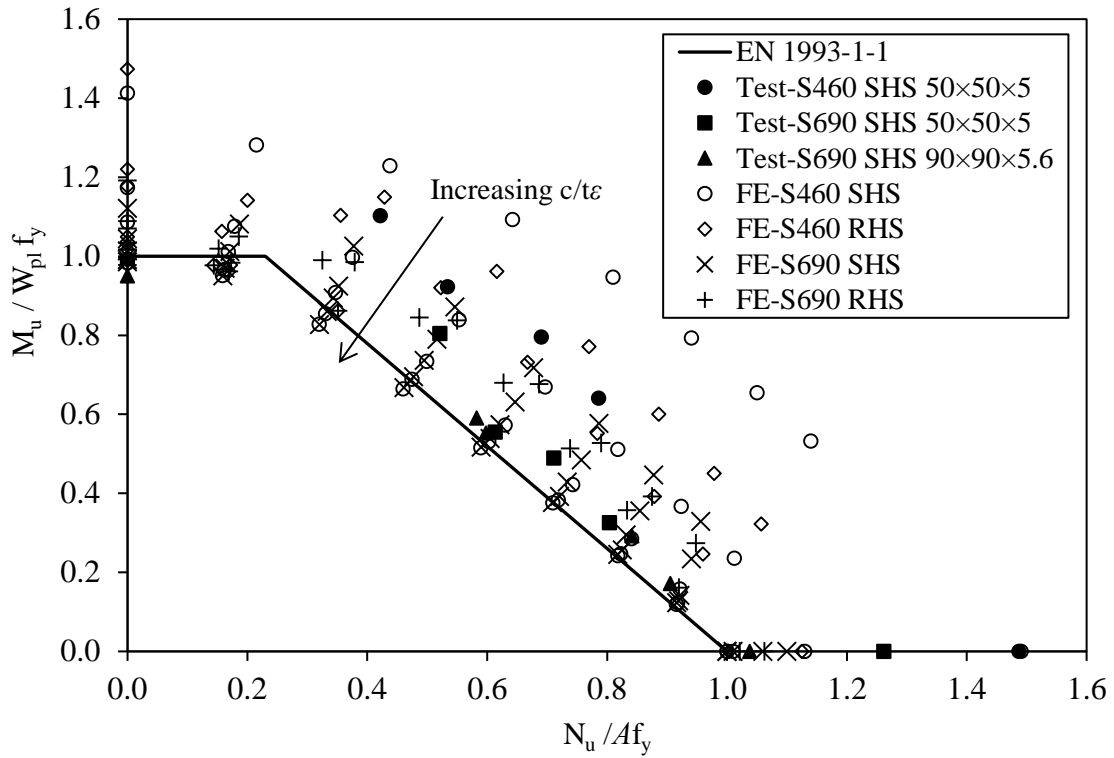
a) SHS and RHS bending about the major axis
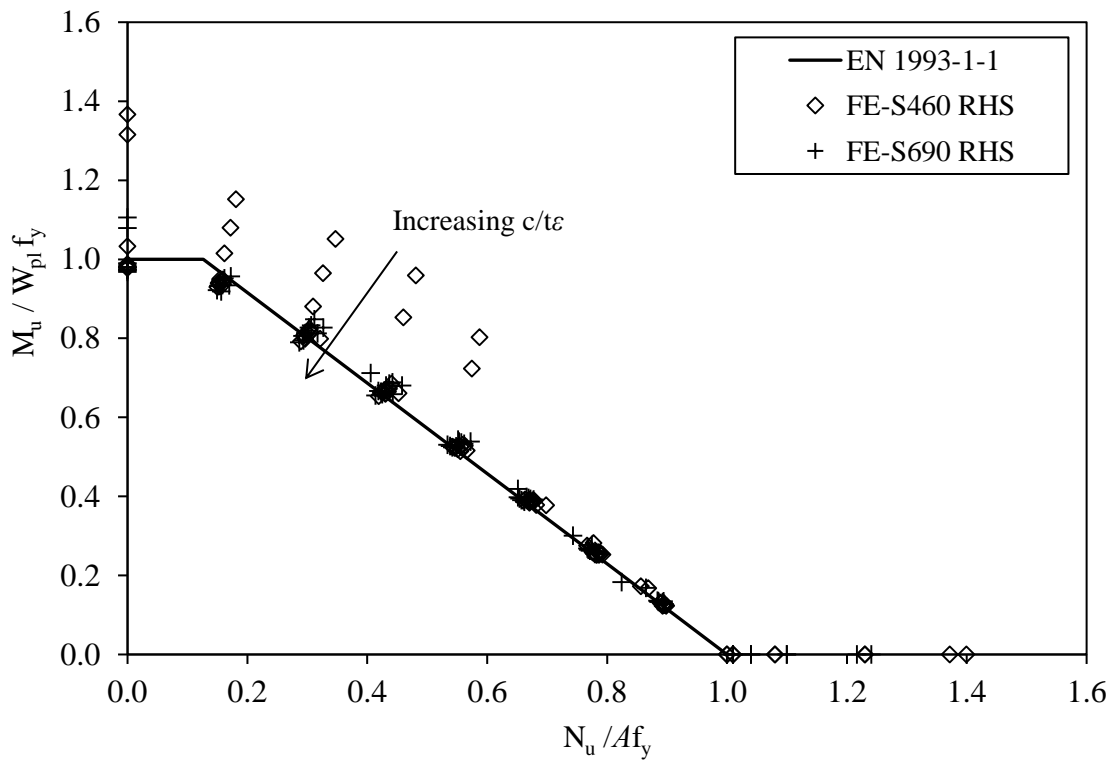
b) RHS bending about the minor axis

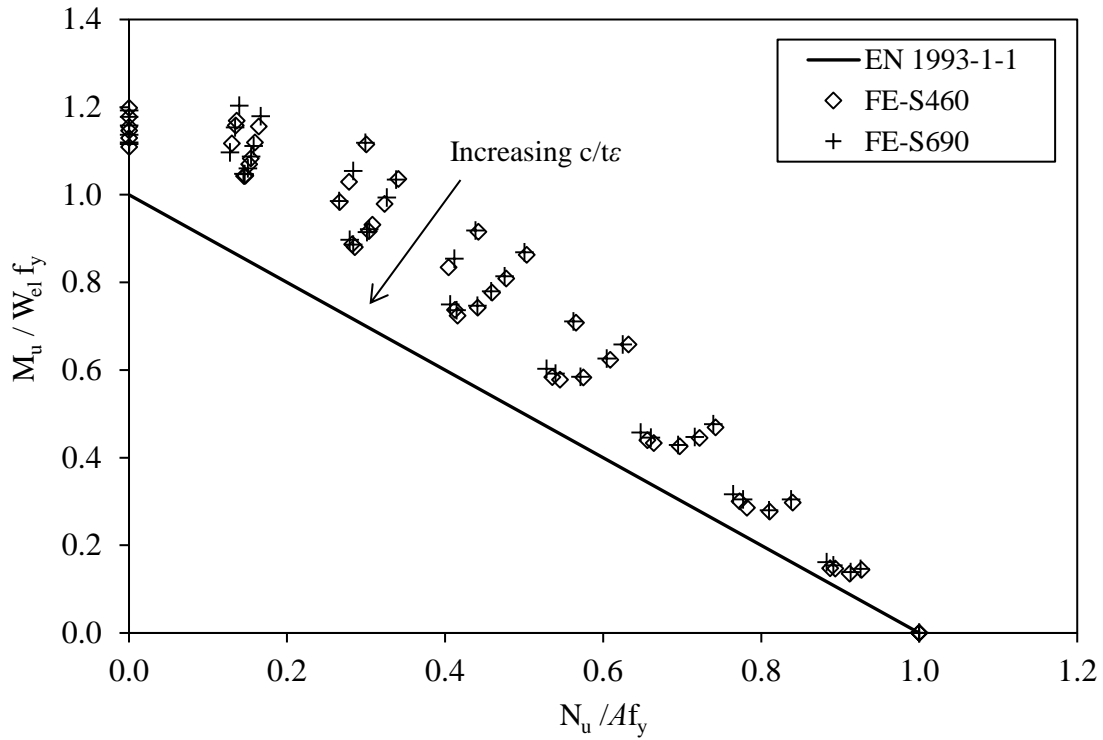**Figure 11:** Assessment of N-M interaction curves for Class 1 and 2 cross-sections

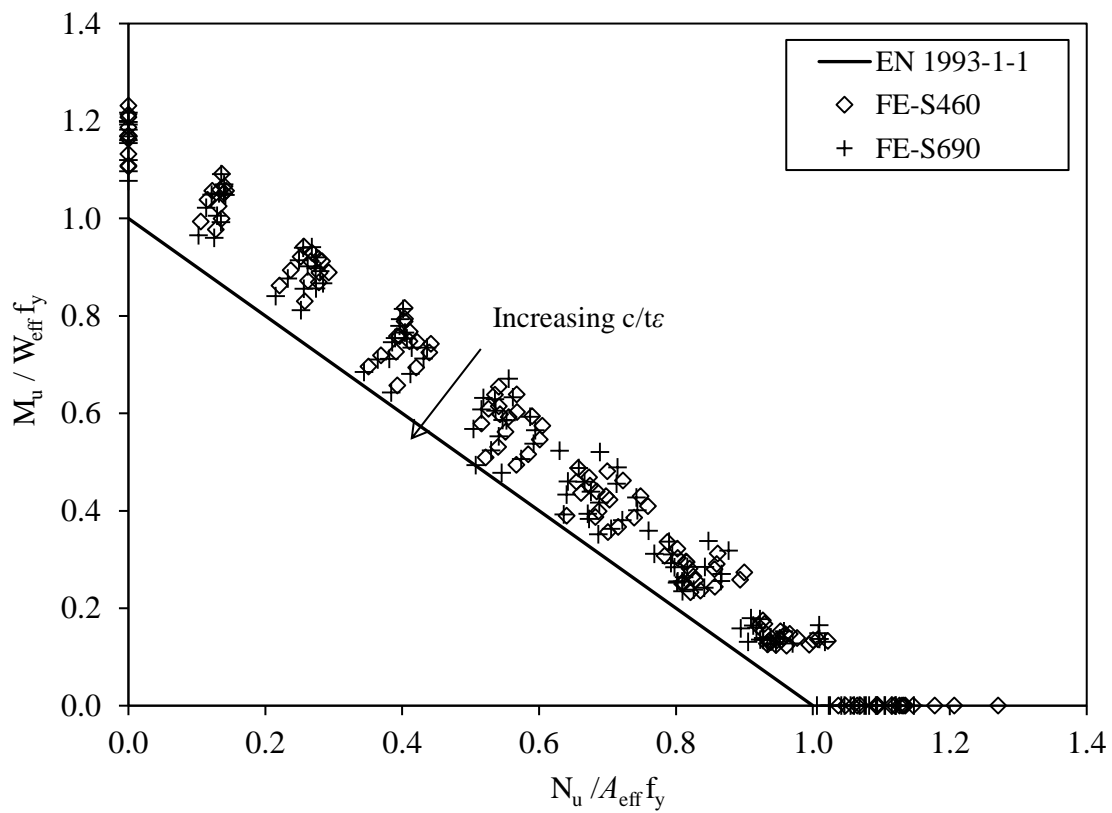**Figure 12:** Assessment of N-M interaction curve for Class 3 cross-sections

Figure 13: Assessment of effective section properties and interaction curves for Class 4 cross-sections
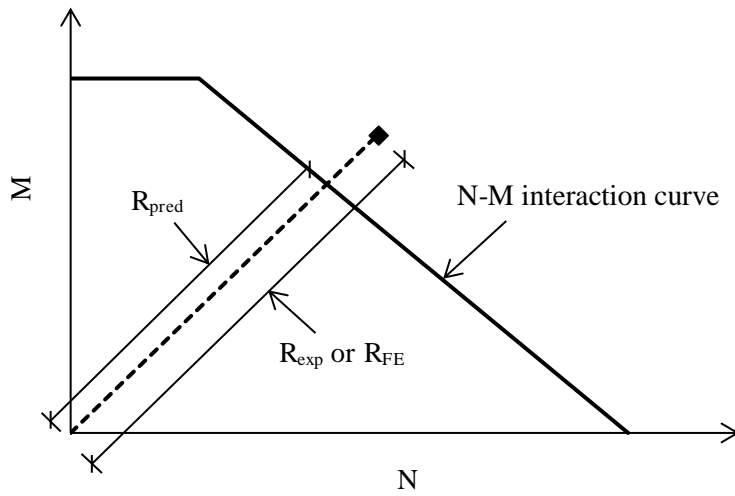
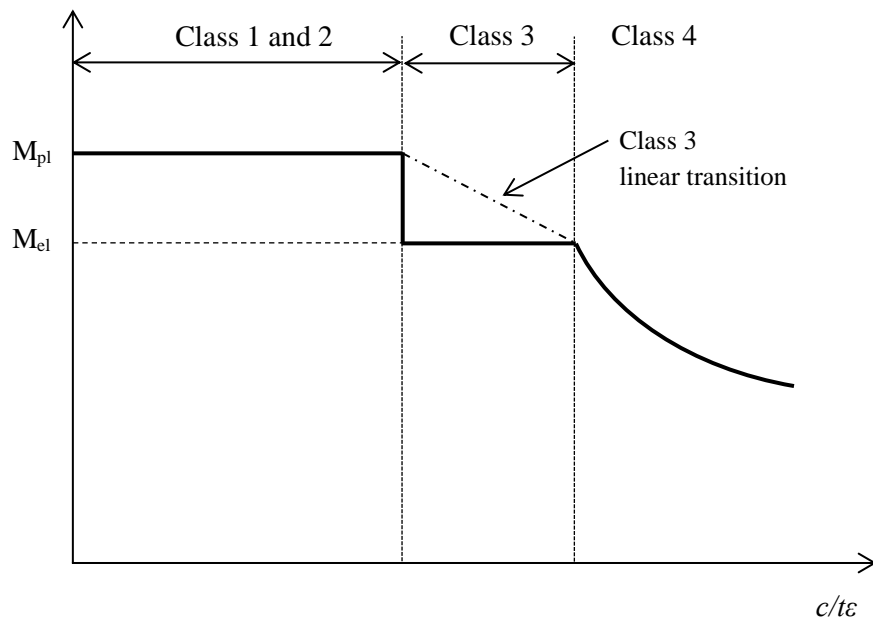**Figure 14:** Definition of utilisation ratio of the test or FE to predicted capacities

Figure 15: Bending resistances for different cross-section classes, including illustration of linear transition for Class 3 cross-sections (after Taras et al., 2013)